

# Cryogenic Thermal Modeling of Microwave High Density Signaling

Naomi Raicu<sup>1</sup>, Tom Hogan<sup>2</sup>, Xian Wu<sup>3</sup>, Mehrnoosh Vahidpour<sup>3</sup>, David Snow<sup>3</sup>, Matthew Hollister<sup>4</sup>, Mark Field<sup>3</sup>

1. *University of Wisconsin-Milwaukee, P.O. Box 413, Milwaukee, WI 53201*

2. *Quantum Design, 10307 Pacific Center Court, San Diego, CA 92121*

3. *Rigetti Computing, 775 Heinz Avenue, Berkeley, CA 94710*

4. *Fermi National Accelerator Laboratory, PO Box 500, Batavia, IL 60510-5011*

(Dated: February 3, 2025)

Superconducting quantum computers require microwave control lines running from room temperature to the mixing chamber of a dilution refrigerator. Adding more lines without preliminary thermal modeling to make predictions risks overwhelming the cooling power at each thermal stage. In this paper, we investigate the thermal load of SC-086/50-SCN-CN semi-rigid coaxial cable, which is commonly used for the control and readout lines of a superconducting quantum computer, as we increase the number of lines to a quantum processor. We investigate the makeup of the coaxial cables, verify the materials and dimensions, and experimentally measure the total thermal conductivity of a single cable as a function of the temperature from cryogenic to room temperature values. We also measure the cryogenic DC electrical resistance of the inner conductor as a function of temperature, allowing for the calculation of active thermal loads due to Ohmic heating. Fitting this data produces a numerical thermal conductivity function used to calculate the static heat loads due to thermal transfer within the wires resulting from a temperature gradient. The resistivity data is used to calculate active heat loads, and we use these fits in a cryogenic model of a superconducting quantum processor in a typical Bluefors XLD1000-SL dilution refrigerator, investigating how the thermal load increases with processor sizes ranging from 100 to 225 qubits. We conclude that the theoretical upper limit of the described architecture is approximately 200 qubits. However, including an engineering margin in the cooling power and the available space for microwave readout circuitry at the mixing chamber, the practical limit will be approximately 140 qubits.

## I. INTRODUCTION

Superconducting quantum computers use qubits with energy gaps between the ground and the first excited states in the microwave regime. Frequencies in this range allow for qubit manipulation and readout using microwave components in the low-photon number regime but also require the devices to be operated at temperatures of order 20 mK so that the thermal population of the first excited state is negligible. Commercially available dilution refrigerators achieve these temperatures, but the system must be engineered such that the total heat load coming from the outside or generated within the cryostat is lower than the cooling power available from the refrigeration system. The qubit gate operation and readout are controlled by microwave pulses generated by room-temperature electronics outside the cryostat. These pulses travel down through signaling cables that are attached at the different temperature stages of the dilution refrigerator. The cables create a static heat load due to thermal conductivity and temperature differences between stages. Any cable that carries a current also has an active load due to Ohmic heating due to the cable resistivity and heat loss in attenuators used to thermalize the cable at each stage [1].

Scaling the number of qubits to the 100-200 range requires an increase in the number of signal lines; however, there is a limit to the number of cables that can be accommodated for any one particular cable type. This limiting factor is usually either the thermal budget or the available space [2]. More compact and dense microwave cable types are being actively investigated [3], and other po-

tential solutions to scaling the number of control signals have been reported, such as using cryo-CMOS circuits either for RF switching [4] or arbitrary waveform generation within the cryostat [5], or using optical fibers and a transducer to create RF pulses from optical signals [6].

This work extends the work of Krinner et al. [2] in modeling the thermal loads resulting from the delivery of signals to superconducting quantum processors. Here, we examine a commonly used small-format coaxial cable: the SC-086/50-SCN-CN semi-rigid coaxial cable used in the Bluefors High-Density Wiring (HDW). These cables have the same internal dimensions as the UT-085 cables considered by [2], with a cupronickel outer and silver-coated cupronickel inner conductor with a PTFE dielectric. Assemblies of these coaxial lines are used in the Bluefors XLD1000-SL range of dilution refrigerators to allow simplified wiring configuration changes.

In this paper, we determine the material composition and cross-sectional dimensions of the different parts of the cable. The thermal conductivity of the various parts was then experimentally measured as a function of temperature, and we then developed a thermal model of the coaxial cable static heat load across all thermal stages spanned by the cable. In addition, we measured the electrical resistivity of the signal line as a function of temperature to estimate the active loads due to Ohmic heating for a single cable. This active load is determined by the system configuration and architecture, where the current in the signal line and the attenuators dissipate heat. Finally, we combine the static and active heat load models to simulate a complete superconducting quantum computer ranging in size from 100 to 225 qubits.

## II. OVERVIEW OF THERMAL MODELING

Current designs of dilution refrigerators are able to cool the sample space to under 20 mK without cryoliquids using a He3/He4 dilution unit that is precooled by a two-stage pulse tube refrigerator [7, 8]. The cables within a dilution refrigerator are thermally anchored at several stages within the fridge whose temperatures are set by the active cooling systems. The nominal stage temperatures and estimated cooling powers for the Bluefors XLD1000-SL system, along with the cable lengths, are shown in Table I. Bluefors specifies the cooling power and base temperature only at the MXC stage [9], and the numbers for higher temperature stages are estimates based on our own experience of running these systems and are indicated by an asterisk in Table I. These cooling powers are those available to cool experimental loads added to the bare refrigerator. The dilution fridge is a coupled dynamic system, and the estimated cooling power of each fridge stage varies according to how the system is operated and optioned, depending on the specifications of the installed pulse tube coolers and the dilution units. Pulse tube technology has improved substantially over the past years, and the available cooling power is expected to increase. For this paper, we assume the system has two Cryomech PT420 pulse tubes, the standard configuration of the Bluefors XLD1000-SL at the time of writing. Bluefors currently has the option to upgrade these to the Cryomech PT425 or PT310 pulse tube configurations for greater cooling power and additional options to have three pulse tubes at the expense of reducing the number of side-loading ports for the wiring [9]. The fridge has multiple wiring options, and here we focus on the SC-086/50-SCN-CN coax cable used in the Bluefors High-Density Wiring (HDW) option.

The calculated static and active heat loads for each model are summed to provide a total input heat load at each stage. The final heat load at each fridge stage is determined by the difference between the incoming heat load from higher temperature stages, the Ohmic heating, and the outgoing load to the next lower temperature stage. This final load is then compared to the estimated cooling power of each fridge stage shown in Table I.

To model a complete superconducting processor, we take a common design that uses flux tunable transmons as the basic qubit design, with tunable couplers between pairs of qubits that are designed for use in two-qubit gate operations [10]. The control and readout lines for these processors can be split into four different categories:

1. Qubit XY drive lines for single-qubit operations.
2. Qubit flux bias lines to set the qubit frequency.
3. Tunable Coupler flux bias lines to set the coupler operating point.
4. Readout lines to excite the readout resonator and perform a measurement on the qubit.

The different functional groups of the microwave lines will each have a different attenuator configuration to ensure the thermal noise on the signal line at the processor is at the fridge’s base temperature. All of the lines provide a static heat load because they run from room temperature to the MXC, while the active Ohmic load depends on the current in the line and the attenuator configuration.

The qubit XY lines carry infrequent microwave pulses for single-qubit manipulation, while the flux bias line has a constant current to set the qubit frequency. The tunable couplers have a similar flux bias line with a constant current to set the operating point so that the two qubits do not interact, which is changed to enable two-qubit gate interactions. Each qubit is coupled to a resonator for readout, and the readout circuit has a read-in line coupled to several resonators and continues on to a read-out line with isolators and amplifiers. A traveling wave parametric amplifier (TWPA) and a low noise semiconductor amplifier are frequently used to boost the output signal in the readout. The TWPA requires a separate microwave line to provide a microwave pump signal, and a semiconductor amplifier will have twisted-pair dc wiring and produce heat that must be accounted for.

Bluefors XLD1000-SL Dilution Refrigerator			
Estimated values configured with two PT-420 pulse tubes			
Refrigerator Stage Name	Nominal Temperature (K)	Cooling Power (W)	Cable Length (m)
300K	297		
50K	40*	30*	0.3053
4K	3.5*	0.7*	0.3155
Still	1.4*	7e-3*	0.2775
CP	0.2*	1e-3*	0.1965
MXC			0.1965
Below MXC	0.02	30e-6	0.1965

TABLE I. Estimated temperatures and cooling power at each refrigerator temperature stage of a Bluefors XLD1000-SL system for a bare fridge. The acronyms “CP” and “MXC” respectively refer to the cold plate and mixing chamber stages of the dilution fridge. Cable lengths refer to the cable run from the higher temperature stage. “Below MXC” refers to the cables run from the MXC to the package holding the quantum processor. The Below MXC cables are not considered in the static heat load as they are isothermal at the mixing chamber temperature. They do, however, contribute an active load. Bluefors specifies the cooling power and base temperature only at the MXC stage [9]; the numbers for higher temperature stages are estimates based on our own experience of running these systems, and they are indicated by an asterisk.

### III. STATIC HEAT LOADS

#### A. Overview of Static Heat Loads

Coaxial cables carry heat from the hotter fridge stages, and each material component has a different thermal conductivity. We model the inner and outer conductors and the dielectric layer of the coaxial cable as separate parallel thermal paths, which we then sum to produce a total static heat load. The model requires the dimensions of the material components, the fixed temperatures at each end of the cable, and each material’s thermal conductivity as a function of temperature.

While comprehensive thermal conductivity functions exist for various grades of copper and aluminum, models for certain cupronickel alloys are not generally available from cryogenic to room temperatures. In this study, we measure the thermal conductivity of the outer and inner conductors of SC-086/50-SCN-CN coaxial cable samples (Coax Co., Ltd.) as a function of temperature from cryogenic to room temperature. For the thermal conductivity of the PTFE dielectric layer, we use the published Teflon  $k(T)$  function from the NIST Cryogenics Index of Material Properties database [11, 12]. While PTFE and Teflon are both ways to refer to Polytetrafluoroethylene, we will refer to this material as “PTFE”.

The static model only considers heat transport by thermal conduction. While infrared radiation is present, the cryogenic temperatures and the low emissivity of the outer conductor of SC-086/50-SCN-CN coaxial cable ensure it is insignificant compared to the thermal conductivity [2]. The only time the correction due to infrared radiation is accounted for is in the experimental measurement of thermal conductivity where the Quantum Design software incorporates an estimate of the radiative losses into the measurement, and thus we must ensure that the emissivity is set to a realistic value.

#### B. Composition and Construction of SC-086/50-SCN-CN Coaxial Cables

The SC-086/50-SCN-CN cable (Coax Co., Ltd.) has a C7150 cupronickel outer conductor, a PTFE dielectric, and a silver-coated (nominal thickness = 3 - 4  $\mu\text{m}$ ) C7150 inner conductor. The material specifications and dimensions are detailed in Table II and are taken from [13].

Fig. 1(a) shows a diagram of the construction of the cable along with nominal dimensions, and Fig. 1(b) and 1(c) shows cross-sectional scanning electron microscope pictures of a cable sample confirming the dimensions, including the thickness of the silver plating on the signal line. The composition of the cupronickel inner and outer conductors, as well as the dielectric, were measured using Energy Dispersive X-ray (EDX) analysis to determine the atomic ratios of materials. Table III gives the measured atomic ratios of copper to nickel for the cupronickel alloy in both conductors, which is approximately 62.5:37.5,

and the measured atomic ratio of carbon to fluorine for the dielectric, which is close to the 1:2 ratio expected from the  $(\text{C}_2\text{F}_4)_n$  molecular structure of PTFE.

SC-086/50-SCN-CN Specifications			
	Diameter (mm)	Cross-Sectional Area ( $\text{mm}^2$ )	Material
Outer	0.86	0.2389	C7150
Dielectric	0.66	0.3098	PTFE
Inner	0.203	0.0324	Ag-Plated C7150

TABLE II. Dimensional and Material Specifications of SC-086/50-SCN-CN Coaxial Cable [13]. The cross-sectional areas of the material in each layer are calculated from the diameters of the different components, subtracting the area of the inner layers for the outer and dielectric layers.

Energy Dispersive X-ray Materials Analysis of SC-086/50-SCN-CN Coaxial Cable				
	Inner Conductor		Outer Conductor	
Element	Wt%	at%	Wt%	at%
C	3.58	16.04	3.46	15.68
Ni	34.50	31.59	34.39	31.59
Cu	61.92	52.37	62.15	52.73
Cu : Ni ratio	62.4 : 37.6		62.5 : 37.5	
Dielectric				
Element	Wt%	at%		
C	23.81	33.1		
F	76.19	66.9		
C : F ratio	33.1 : 66.9			

TABLE III. Compositional analysis of the inner and outer conductors and the dielectric layer, measured by EDX on the cross-sectional sample shown in Fig. 1. For the inner conductor measurement, the electron probe was far away from the silver coating, which excluded silver from the analysis. The Cu:Ni ratio is approximately 62.5:37.5 in the two conductors. In the dielectric, the carbon-fluorine ratio is close to the theoretical value of 1:2 from the molecular structure  $(\text{C}_2\text{F}_4)_n$ .

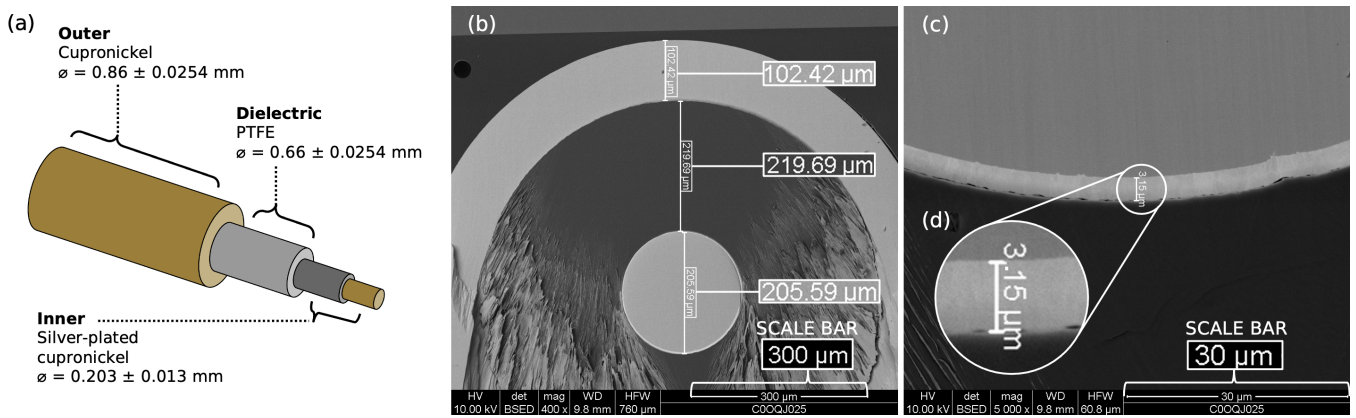


FIG. 1. (a) Depiction of the layers (not to scale) of an SC-086/50-SCN-CN coaxial cable (Coax Co., Ltd.) with materials and dimensions taken from the manufacturers' website [13]. (b) The SEM cross-section of an SC-086/50-SCN-CN coaxial cable sample from Coax Co., Ltd. has measured dimensions that agree with the reported dimensions in 1(a). Measured dimensions and scale are enlarged for readability. (c) A higher magnification image of the inner conductor of an SC-086/50-SCN-CN coaxial cable sample. The measured silver coating is approximately  $3 \mu\text{m}$  thick, which agrees with the nominal thickness reported in [13]. Measured dimensions and scale are enlarged for readability. (d) An enlarged portion of 1(c) to make the dimension of the silver coating readable. A larger decimal point was digitally added to the image for clarity.

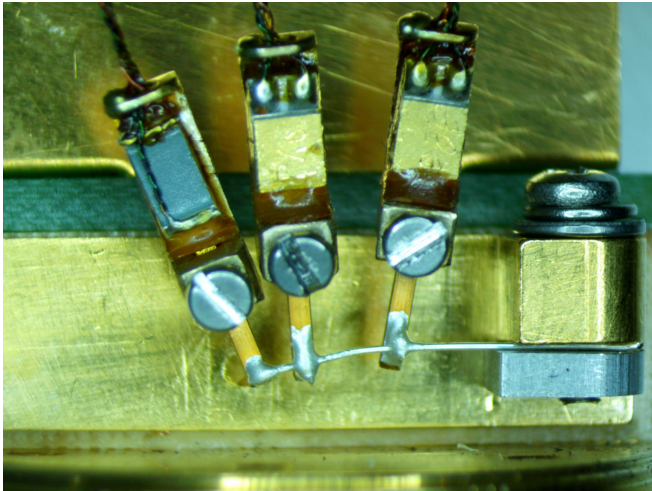


FIG. 2. The cupronickel outer conductor of an SC-086/50-SCN-CN coaxial cable mounted on the PPMS TTO measurement system, showing the sample heater at the left used by the system to produce a time dependent thermal gradient across the sample, followed by two thermometers. The sample is thermally anchored at the right-hand end.

### C. Experimental Measurement of Thermal Conductivity

A sample of SC-086/50-SCN-CN coaxial cable was deconstructed into its three constituent components: the C7150 cupronickel outer conductor, the PTFE dielectric, and the silver-coated C7150 cupronickel inner conductor.

The thermal conductivity of the outer and inner conductors were each measured using the Thermal Transport Option (TTO) in a DynaCool Physical Property Measurement System (PPMS) by Quantum Design, Inc.

[14, 15]. Using this method, the thermal conductance of the sample is measured and then converted to thermal conductivity based on the temperature sensor lead separation, cross-sectional area, and emissivity.

The TTO measurement setup, shown in Fig. 2, involves the connection of an electrical heater to the free end of a sample and the thermal anchoring of the other end to a variable temperature stage. The heater is operated in a pulsed mode, and two thermometers placed along the sample measure the local temperature. Fitting the rise and fall of the temperature change versus time allows the thermal conductance to be extracted [14]. The sample emissivity is a parameter of the thermal model, which includes an estimate of the radiative heat loss.

Samples were measured in the “continuous” measurement mode over a 2 - 300 K temperature range. Inner conductor lead separation was measured to be 2.69 mm, while outer conductor lead separation was 6.96 mm. The inner conductor cross-section was estimated to be  $0.0324 \text{ mm}^2$ , given the reported 0.203 mm outer diameter of the circular inner conductor. The outer conductor cross-section was estimated to be  $0.2389 \text{ mm}^2$ , given the annular shape of the outer conductor cross-section and given the reported 0.86 mm outer diameter of the outer conductor and the reported 0.66 mm outer diameter of the dielectric layer. The cross-sectional dimensions of the cable are summarized in Table II.

The correction for radiative losses is largest at higher temperatures, even though, in this case, it remains a small correction [2]. For the emissivity input for these corrections, we selected fixed emissivity values measured at 300 K from the literature, the highest temperature at which we measured thermal conductance. Although emissivity is known to vary with temperature, there is only a slight variation over the range 300 - 50 K where

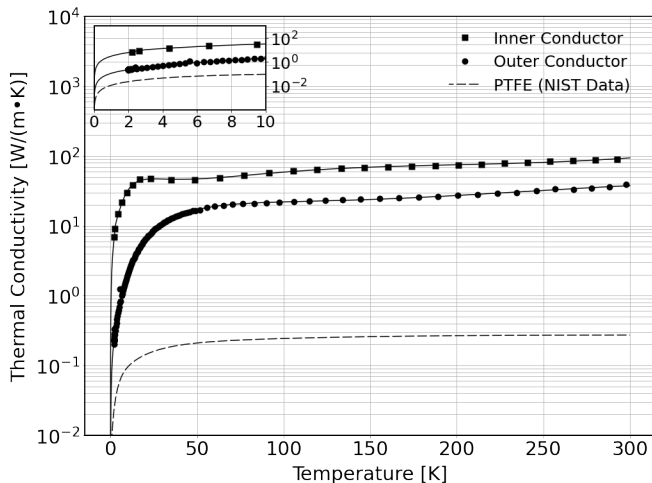


FIG. 3. Thermal conductivity versus temperature for silver-coated cupronickel inner conductor, cupronickel outer conductor, and PTFE. Due to the challenge in accurately modeling the radiative correction above 300 K, the raw data was processed to exclude points above 300 K; the curves shown fit the processed data. The PTFE function displayed is the Teflon model from the NIST Cryogenics Index of Material Properties database [11, 12].

the correction for radiation losses is typically significant compared to the sample thermal conductance. The inner conductor has a  $3 \mu\text{m}$  silver coating, and the emissivity is taken to be  $\epsilon = 0.00775$ , from the measured emissivity at 300 K of a silver coating ( $> 5 \mu\text{m}$ ) on a polished SS304L stainless steel surface reported by Woods et al. 2014 [16]. The outer conductor is a cupronickel alloy of 62.5:37.5 Cu to Ni ratio. The emissivity value is taken to be  $\epsilon = 0.0813$  based on a curve fit of emissivity versus composition of cupronickel alloy reported in Gelin et al. 2004, where they refer to this emissivity as “thermal emittance” [17].

Experimental thermal conductivity data for the inner and outer conductors is shown in Fig. 3, along with a PTFE thermal conductivity curve supplied by the NIST Cryogenics Index of Material Properties database [11, 12].

#### D. Fitting the Thermal Conductivity of SC-086/50-SCN-CN Components

The inner and outer conductor PPMS TTO thermal conductivity data are shown in Fig. 3. Each processed dataset was fitted using a least-squares polynomial fitting procedure to obtain a smooth  $k(T)$  function valid for temperatures shown in the equation range row in Table IV. To process the data, measurements performed above 300 K were discarded due to the challenge in accurately modeling the radiative correction above 300 K.

The  $k(T)$  fit function is based on an 8th-degree Taylor series of the base-10 logarithm of temperatures  $T$ , a for-

mat used in the NIST cryogenic database. The utility of this particular format lies in the fact that it can handle functions that change many orders of magnitude:

$$k(T) = 10^c [a + b(\log_{10} T) + c(\log_{10} T)^2 + d(\log_{10} T)^3 + e(\log_{10} T)^4 + f(\log_{10} T)^5 + g(\log_{10} T)^6 + h(\log_{10} T)^7 + i(\log_{10} T)^8] \quad (1)$$

The least-squares fitting procedure determined the value of alphabetical coefficients  $a$  through  $i$  in equation (1). These coefficients were used to plot the smooth inner and outer conductor thermal conductivity curves shown in Fig. 3. Similarly, the coefficients provided by the NIST Cryogenics database for PTFE were used to plot the thermal conductivity over the range 4 - 300 K.

Thermal Conductivity Fit (W/(m·K))			
Coefficient	Outer	Dielectric	Inner
a	-3.198	2.7380	-2.750
b	20.499	-30.677	25.845
c	-66.114	89.430	-74.184
d	117.690	-136.99	113.586
e	-121.477	124.69	-96.844
f	76.215	-69.556	46.383
g	-28.749	23.320	-11.825
h	5.985	-4.3135	1.322
i	-0.527	0.33829	-0.025
Valid equation range	2.0 - 297.6 K	4 - 300 K	2.3 - 292.6 K

TABLE IV. Fitting coefficients for thermal conductivity as a function of temperature. “Inner” coefficients fit our  $k(T)$  data for the silver-coated C7150 inner conductor of an SC-086/50-SCN-CN cable, and “outer” coefficients fit our  $k(T)$  data for the C7150 outer conductor for the same cable. “Inner” and “outer” coefficients were rounded to the nearest thousandth. Data points collected for the inner and outer conductors correspond to temperatures that range from approximately 2.0-297.6 K for the outer conductor and approximately 2.3-292.6 K for the inner conductor. Polynomial fits were used to calculate thermal conductivity for temperatures in the reported ranges for each material and up to 300 K. A linear extension to the origin from the data point corresponding to the lowest temperature in the set of used points was used for modeling thermal conductivities at low temperatures. PTFE coefficients are sourced from the NIST Cryogenics Index of Material Properties database [11, 12].

Since our work requires thermal conductivities down to 20 mK, we need to extend the fits below the lower end of the experimental data and the validity of the power series function. Here we assume that the thermal conductivity of materials goes to zero at zero temperature, and we extend the thermal conductivity curve using a straight line that connects the lowest-temperature experimental

$k$  data point down to the origin. This procedure likely overestimates the thermal conductivity in this temperature range as the slope of the experimental data near the lowest temperatures is larger than the slope of the straight-line approximation.

Table IV shows the fitting coefficients  $a$  through  $i$  for the outer and inner conductors as determined by the least-squares polynomial fit. The coefficients were used to graph the solid black curves of best fit for the inner and outer conductor data in Fig. 3. The NIST PTFE curve was plotted using the coefficients available from the NIST Cryogenics Index of Material Properties database [11, 12].

### E. Method of Calculating Static Heat Load

We model the coaxial cable as three parallel thermal conductances, one for each cable component: the outer conductor, dielectric, and inner conductor. The total thermal conductance of the cable is then the sum of each component's conductance.

While our model does not assume that the temperature profile along any one cable component exactly matches another, it ignores any radial heat transfer across the cable. We justify this simplification by pointing out that the cable's construction is such that the two conductors are separated by a low thermal conductivity dielectric, an arrangement that limits the radial heat flow. Radial heat flow becomes more relevant in the case of significant Ohmic heating due to a large current flow in the cable where the inner and outer conductors might have very different temperatures.

If the cable components have a constant cross-sectional area and length, the static heat load associated with a given cable component can be calculated by numerically integrating over the thermal conductance for that material as a function of temperature using a fit to the function such as those discussed in Section III D:

$$q_{component} = \frac{A}{L} \int_{T_L}^{T_H} k(T) dT \quad (2)$$

Where  $q_{component}$  is the static heat load of the cable component,  $T_L$  and  $T_H$  are the low and the high temperatures spanning either end of a section of cable,  $A$  is the cross-sectional area,  $L$  is the length of the cable section, and  $k(T)$  is the thermal conductivity of the component material as a function of temperature  $T$ .

We sum the static heat load associated with each cable component - the outer conductor, dielectric, and inner layers - to determine the total static heat load for a single cable:

$$q_{cable} = \sum q_{component} = q_{outer} + q_{dielectric} + q_{inner} \quad (3)$$

Where  $q_{outer}$ ,  $q_{dielectric}$ , and  $q_{inner}$  respectively refer to each static heat load associated with the components of a coaxial cable.

The calculated static heat loads of a single SC-086/50-SCN-CN cable in the Bluefors XLD1000-SL system, with the stage temperatures and line lengths given in Table I, are shown in Table V.

Calculated Static Heat load of a Single SC-086/50-SCN-CN coaxial cable	
Fridge Stage	Static Heat Load (W)
50K	7.566e-03
4K	3.157e-04
Still	2.373e-06
CP	5.491e-07
MXC	1.132e-08

TABLE V. The calculated static heat load of a single SC-086/50-SCN-CN coax cable in a Bluefors XLD1000-SL system at each fridge stage.

We calculate  $q_{stage}$ , the total static heat load of  $N$  cables into a dilution refrigerator temperature stage, for each refrigerator temperature stage by multiplying  $q_{cable}$  by the number of cables  $N$ .

The maximum number of Bluefors HDW SC-086/50-SCN-CN cables currently available in a Bluefors XLD1000-SL system is  $N = 1008$  [18]. We calculated the fraction of the available cooling power at each stage by taking the ratio between  $q_{stage}$  and the cooling power at each stage as listed in Table I. The results are plotted as a bar chart in Fig. 4 and show that the largest fractional heat load is surprisingly not at the mixing chamber but at the cold plate where the cables take up 64.8% of the available cooling power. There is a sufficient engineering margin for the mixing chamber to reach the base temperature. Using superconducting cables below the 4K stage in place of SC-086/50-SCN-CN would reduce this load dramatically.

## IV. ACTIVE HEAT LOADS

### A. Overview of Active Heat Loads

All cables carrying an appreciable current will produce an Ohmic heat load within the cryostat. In addition to the resistance of the cable, the heat load in the attenuators used to thermalize the signal line must also be accounted for. Thermalization of the signal line is required to reduce the blackbody radiation present in the cables to a level corresponding to a thermal photon occupation number typically taken to be  $\approx 10^{-3}$ , requiring a total attenuation of at least 60 dB [2]. The effects of thermally generated electrical noise in cables and components on qubit dynamics are examined in [19, 20]. In-

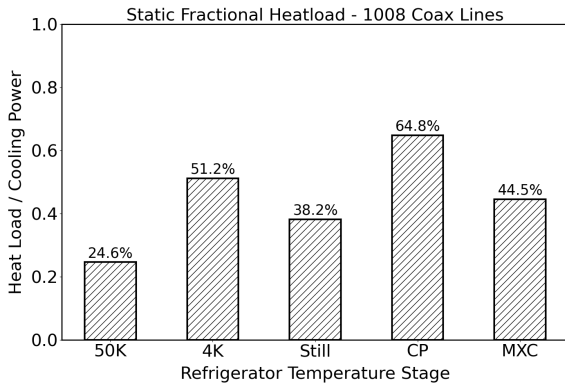


FIG. 4. The fraction of the estimated cooling powers at each stage taken up by static heat loads of a Bluefors XLD1000-SL system outfitted with the maximum number of cables ( $N = 1008$ ). The different refrigerator temperature stages on the x-axis are, as before, denoted as follows: “50K” for the 50K plate, “4K” for the 4K plate, “Still” for the still stage, “CP” for the cold plate, and “MXC” for the mixing chamber.

frared filtering elements are also included in the coax line to prevent radiation from higher temperature stages from propagating through the dielectric layer.

The active load in a coaxial cable is distributed along the cable, but the heat flows predominantly to the lower-temperature end of the cable, where it adds to the static heat load. Due to its smaller cross-sectional area, the inner conductor of the cable has a significantly higher resistance compared with the outer conductor; in our active load model, we only consider the Ohmic heating in the inner conductor. The return currents flow through the much lower-resistance outer conductor and the fridge mounting hardware, which is electrically connected to the grounds of the cables [2]. In the next section, we measure the inner conductor’s DC electrical resistivity as a function of temperature, which is then used as an input to the active thermal model.

A superconducting quantum computer typically has other sources of heat within the cryostat beyond the active loads in the cables and attenuators, such as semiconductor amplifiers at the 4K stage and TWPA amplifiers at the mixing chamber with a microwave pump signal that is terminated in a  $50 \Omega$  load. The active load thermal models depend on the system configuration and the current in the signal lines. Due to the limited available cooling power, the fraction of available MXC cooling power taken up by the processor is particularly sensitive to the resistance of the cables and the connections to the package holding the quantum processor at the mixing chamber stage. In addition to the limited cooling power, generating heat near the quantum processor creates potential problems as the processor package could become locally hotter than its surroundings unless the processor has an adequate thermal connection to the mixing chamber, something that the available thermometers might

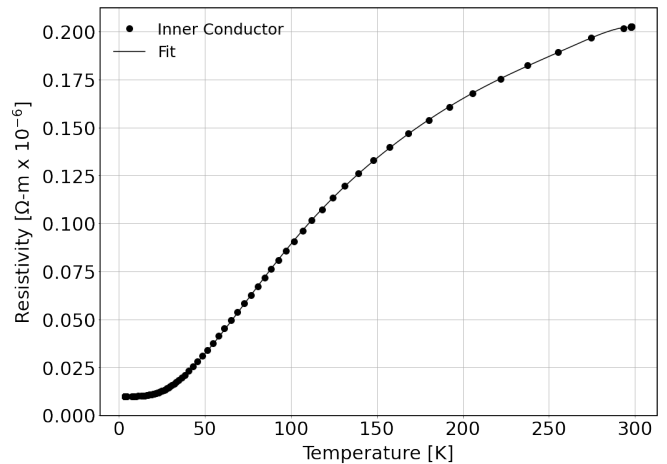


FIG. 5. DC electrical resistivity versus temperature for the silver-coated cupronickel inner conductor. The data was scaled by the cross-sectional area and length of the cable to give resistivity values.

not pick up. The static heat load models do not need to include the processor connections at the mixing chamber as all of those cables are isothermal to the MXC plate, and hence, there is no static load below the MXC.

## B. Experimental Measurement of DC Resistivity

We measured the DC electrical resistivity of the inner conductor of an SC-086/50-SCN-CN cable between room temperature and 3.8 K as determined by a Cernox temperature sensor. A 0.254 m (10”) length of SC-086/50-SCN-CN coaxial cable was mounted on the 4K stage of a dilution refrigerator by connecting the two ends to two SMA feedthroughs on a KF-40 flange. This guarantees the efficient thermalization of the cable the same way the coaxial cables are anchored to the flanges in conventional coaxial builds in dilution refrigerators. The cable is looped back on itself so that both ends are attached to the 4K stage, ensuring that the length of the cable is isothermal to the 4K plate. The resistance was then measured when cooling down and warming up the fridge using a four-terminal setup through a micro-D connector compatible with the DC looms inside the dilution refrigerators. The resistance data was then scaled by the known length and cross-sectional area to give the resistivity and fitted by an eighth-order polynomial.

The data and fit are shown in Fig. 5, and the fit coefficients are shown in table VI. The eight-order fit is in the same functional form as that used for thermal conductivity, i.e.,

DC Electrical Resistivity Fit ( $\Omega\cdot m$ )	
Coefficient	Inner Conductor
a	-8.327
b	10.012
c	-52.833
d	122.547
e	-152.760
f	109.033
g	-44.416
h	9.598
i	-0.854
Valid equation range	3.8 - 300 K

TABLE VI. DC electrical resistivity fit parameters for the inner conductor. The resistivity at temperatures below 3.8 K is taken to be a constant of  $\rho = 9.928e-9 \Omega\cdot m$ .

$$\rho(T) = 10^9 [a + b(\log_{10} T) + c(\log_{10} T)^2 + d(\log_{10} T)^3 + e(\log_{10} T)^4 + f(\log_{10} T)^5 + g(\log_{10} T)^6 + h(\log_{10} T)^7 + i(\log_{10} T)^8] \quad (4)$$

The resistivity approached a constant value below approximately 10 K, the temperature below which the resistivity is dominated by impurity scattering in the metal, and we observe that this value remains constant down to the base temperature of the fridge when the cable is moved to the MXC. Below the fitting temperature range of  $T = 3.8$  K, we use a constant resistivity value of  $\rho = 9.928e-9 \Omega\cdot m$ . We note that RF resistivity will be dominated by the skin effect in the silver coating and will be different from the measured DC resistivity reported here.

### C. Active Load Thermal Model

A substantial portion of active heating within a superconducting quantum computer comes from lines with a significant current for long periods, such as flux bias control lines. Meanwhile, lines carrying low, infrequent, short-duration pulses, e.g., one-qubit gate pulses on the XY control lines and readout pulses on the read-in and read-out lines, contribute little to the thermal loads. Flux tunable qubits require a constant offset to set the detuning of their frequency to neighboring qubits and to compensate for both fabrication spread in the Josephson junction, which leads to an offset in Josephson inductance, and for any stray magnetic flux in the SQUID loop. Tunable couplers require a flux bias current to set the operating point where the coupling between adjacent qubits is zero. For the control lines in the active model,

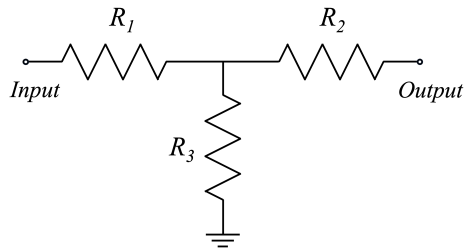


FIG. 6. Circuit diagram for a T-Pad attenuator. Matching the characteristic impedance of the input and output along with the required attenuation allows the three resistor values to be determined, which in this case gives  $R_1 = R_2 = 40.91 \Omega$  and  $R_3 = 10.1 \Omega$  for 20 dB of attenuation.

we consider only the tunable coupler and qubit flux bias signal line currents.

The mean value of flux bias currents for qubits and tunable couplers in a system depends on the design, and measured values should be used to model a real system. For this work, both the qubit flux bias and tunable coupler flux bias lines are estimated to carry a DC current of  $I = 0.4$  mA. This current is estimated from the mutual inductance between the flux bias line and the qubit of  $M = \partial\Phi/\partial I = 0.5\Phi_0/\text{mA}$ , where  $\Phi_0$  is the superconducting flux quantum, and a required flux amplitude of  $\pm 0.2\Phi_0$  [2].

The qubit and tunable coupler flux bias line are configured with attenuation at particular fridge stages to ensure the inner signal line is well thermalized to the cooling system [21]. Each attenuator will dissipate power in the resistors that must be included, feeding only a fraction of the input current to the control line below the attenuator. For this model, we assume an attenuator configuration of a single 20 dB attenuator at the 4K stage of the dilution fridge [2] using a ‘‘T-pad’’ attenuator shown in Fig. 6. Matching the  $50 \Omega$  characteristic impedance of the lines along with the required attenuation allows the three resistor values to be determined, which in this case gives  $R_1 = R_2 = 40.91 \Omega$  and  $R_3 = 10.1 \Omega$  for 20 dB of attenuation. The microwave calibration of attenuators in a typical signal line at cryogenic temperatures has been reported in [22].

Since the output current is smaller than the input current at an attenuator, it is necessary to start with the current required at the lowest temperature stage and work backward up the cable, calculating the input current required to produce the desired output current at each attenuator. We can then use these current calculations, along with measures of cable resistivity and the known resistors in the attenuator, to calculate the active heat load in each line. The assumptions on line currents and attenuator configuration are summarized in Table VII.

Other heat sources within the cryostat must be added to the total heat loads. TWPA amplifiers [23] used in the readout circuit at the MXC stage require an RF pump signal that terminates at a  $50 \Omega$  load. We assume



Active Heat Load Line Currents and Attenuation		
Qubits		
Line Type	Attenuation	Current (mA)
XY Drive	*	0
Flux Bias	20 dB 4K	0.4 at MXC
Tunable Couplers		
Line Type	Attenuation	Current (mA)
Flux Bias	20 dB 4K	0.4 at MXC
Readout Circuit - 6 way multiplexed		
Line Type	Attenuation	Current (mA)
Read In	*	0
Read Out	0 dB	0

TABLE VII. A summary of the signal lines showing the attenuation configuration and current in each of the various lines, also shown in Fig. 7. An asterisk in the attenuation column indicates that while that line does have attenuators, they are irrelevant for the active load model as the line carries negligible current.

Other Active Heat Loads	
TWPA Pump	
Power at TWPA	-60 dBm
Power at directional coupler	-40 dBm
RMS current into 50 $\Omega$ load	0.044 mA
TWPA Pump Attenuation	10 dB at 4K
	10 dB at Still
	10 dB at CP
LNA Power	
Dissipated at 4K Stage	7.8 mW

TABLE VIII. A summary of other active heat loads within the cryostat. Each read-out line has a TWPA with its own pump line and an LNA at the 4K stage. We estimate the RMS current in the TWPA pump line to be the current required to dissipate the TWPA pump power at the input of the 20 dB directional coupler into a 50  $\Omega$  load.

a typical TWPA pump drive of -60 dBm [24], fed by a 20 dB directional coupler. The TWPA pump RF power at the input to the directional coupler will, therefore, be -40 dBm, and the vast majority of that power will go straight through and be dissipated in the 50 Ohm load. The power dissipation allows the RMS current in the pump line at the input to the directional coupler to be calculated to be  $I = 0.044$  mA. Another heat source is from the semiconductor LNA amplifiers that are used in the readout circuit at the 4K stage. A typical LNA that operates over the 4-8 GHz band commonly used in readout dissipates 7.8 mW of power at the 4K stage [25]. The assumptions on TWPA pump and LNA loads are summarized in Table VIII.

#### D. Method of Calculating Active Heat Load

The active heat load is calculated by numerically integrating the resistance value along a cable multiplied by the square of the current. At any stage with an attenuator, the heat load due to the attenuator is given by the sum of the heat loads in the three resistors making up the T-pad attenuator, taking into account the different currents flowing in each. The total active heat load is assumed to flow to the lower fridge stage it is thermally anchored to, so the load quoted for each stage is the active load from the cable above it and the load from the attenuator if one is installed.

The output of the thermal model is a set of thermal heat loads at each fridge stage, which the cooling system needs to handle. This analysis assumes the available cooling power and the operational temperature of fridge stages are fixed, while in reality, these operating points are coupled, which a complete model of a dilution refrigerator could capture.

#### E. Active Load Example in a Bluefors XLD1000-SL Dilution Refrigerator

For this example, we will take a typical attenuation configuration with 20 dB attenuation at the 4K plate of the fridge [2] and the line lengths from a Bluefors XLD1000-SL system detailed in Table I. Using the experimentally determined cable resistivity and a flux bias current of  $I = 0.4$  mA, the calculated active heat loads of a single SC-086/50-SCN-CN cable in the Bluefors XLD1000-SL system are shown in Table IX.

Calculated Active Heat load of a Qubit Flux Line				
Single SC-086/50-SCN-CN coaxial cable				
Input Parameters			Heat Load	
Fridge Stage	Attenuation (dB)	Current In (mA)	Coax (W)	Attenuator (W)
50K	-	2.029	4.157E-6	-
4K	20	2.029	6.903E-7	2.018E-4
Still	-	0.400	1.515E-8	-
CP	-	0.400	1.120E-8	-
MXC	-	0.400	1.084E-8	-

TABLE IX. The calculated active heat load of a simulated qubit flux bias line in a Bluefors XLD1000-SL system. This single SC-086/50-SCN-CN coaxial cable carries 0.4 mA of current at the MXC with 20 dB of attenuation installed at the 4K stage.

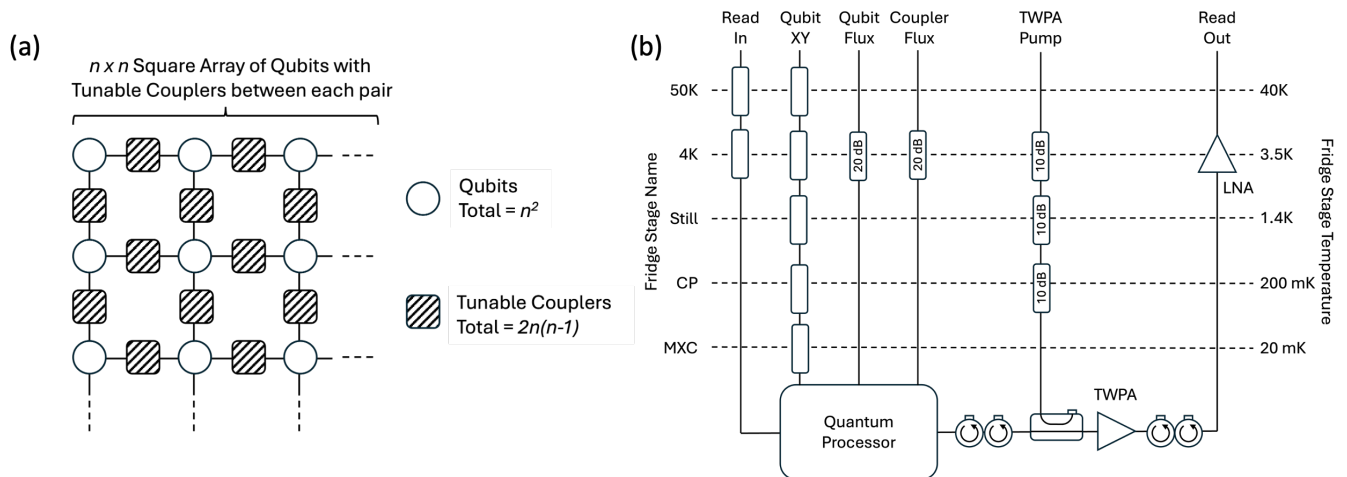


FIG. 7. (a) Diagram showing the layout of the model systems considered in this thermal model with a square array of  $n \times n$  flux tunable transmons and a tunable coupler between each pair of transmons. Each model has  $n^2$  transmons and  $2n(n-1)$  tunable couplers. (b) The fridge wiring diagram of the model system shows the assumed attenuator configuration for each type of line at each fridge stage and the readout chain electronics, including TWPA and LNA amplifiers at the MXC and 4K stages, respectively. Note that the attenuators in the Read-In and Qubit XY lines are just shown without values because they are irrelevant to the thermal model.

Model Quantum Processor Sizes							
Array Size	Components		Circuits	Control Lines			
	Qubits	Tunable Couplers	Readout	Qubits	Tunable Couplers	Readout	Total
$n \times n$	$n^2$	$2n(n-1)$	$\text{ceil}(n^2/6)$	$2n^2$	$2n(n-1)$	$3 \text{ceil}(n^2/6)$	
$10 \times 10$	100	180	17	200	180	51	431
$11 \times 11$	121	220	21	242	220	63	525
$12 \times 12$	144	264	24	288	264	72	624
$13 \times 13$	169	312	29	338	312	87	737
$14 \times 14$	196	364	33	392	364	99	855
$15 \times 15$	225	420	38	450	420	114	984

TABLE X. The sizes of the different model quantum processors considered. Each processor is assumed to be an  $n \times n$  square array containing  $n^2$  qubits, with tunable couplers between each pair of qubits. Each qubit requires two control lines: the XY drive and flux bias lines, while the tunable couplers require a single flux bias line each. The readout circuit requires three lines: a read-in line, a read-out line, and one line for the TWPA pump, and is assumed to be six-way multiplexed. The next entry in the table would be a  $16 \times 16$  array with 256 qubits, but this would require a total of 1121 lines, which is beyond the capacity of  $N = 1008$  lines available in the dilution fridge. Each thermal model assumes that only these lines are present and there are no unused lines in the system.

## V. APPLICATION OF THE THERMAL MODEL TO A BLUEFORS XLD1000-SL DILUTION REFRIGERATOR

This section estimates the full thermal load of different-sized quantum computers with between 100 and 225 qubits installed in a Bluefors XLD1000-SL dilution refrigerator. It does not use the full number of cables the fridge can support. Rather, it estimates real systems using only those signal cables needed that the available cooling power could accommodate.

The model quantum processors are shown in Fig. 7(a) and consist of a square array of  $n \times n$  flux tunable trans-

mon qubits, where  $n = 10, 11, \dots, 15$ , with tunable couplers between each pair [10]. Each model quantum processor has  $n^2$  qubits, and  $2n(n-1)$  tunable couplers. Each transmon is assumed to require two control lines - a flux bias line and an XY drive line - and is also coupled to its own output resonator. Each tunable coupler has its own flux bias line. Model processors with an array of up to  $15 \times 15 = 225$  qubits can be accommodated in the fridge, since a  $16 \times 16$  array with 256 qubits would require a total of 1121 lines, which is beyond the capacity of  $N = 1008$  lines available.

Each readout circuit has a read-in line to the on-chip resonators that continues to a readout line with isola-

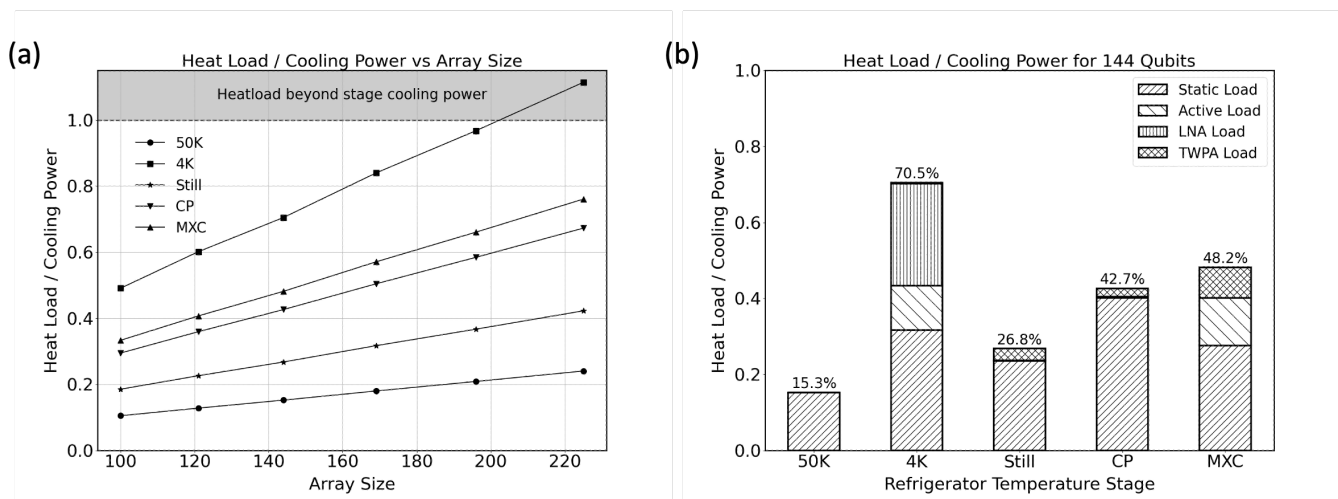


FIG. 8. (a) The fraction of the estimated cooling powers at the different fridge stages used by the total heat loads for model quantum processor configurations of various sizes. (b) An example of the fraction of the estimated cooling powers used at each stage for a 144 qubit processor.

tors, TWPA [23, 26, 27] fed by a pump line coming into a directional coupler, and a semiconductor LNA at the 4K stage. The readout chain assumes six-way multiplexing of the readout resonators onto  $\text{ceil}(n^2/6)$  separate readout circuits, where  $\text{ceil}$  is the ceiling function, which rounds a fraction up to the next integer. Each of the readout circuits requires three microwave lines: one read-in, one read-out, and one line for the TWPA pump. When  $n^2$  is not a multiple of six, one readout circuit will have fewer than six qubits on it. Real designs of processors usually pick the number of qubits to be a multiple of the readout multiplexing to simplify routing, whereas these model processors are just selected to illustrate the scaling of the thermal load. Fig. 7(b) shows the fridge wiring diagram of the model system with the assumed attenuator configuration for each type of line at each fridge stage and the specifics of the readout chain electronics, including TWPA and LNA amplifiers at the MXC and 4K stages, respectively.

The total number of lines for each component in the different-sized models is shown in Table X. Each thermal model assumes that only these lines are present and there are no unused lines in the system. Note that practical wiring configurations usually come in groups of cables determined by the feedthroughs at the flanges, so a real configuration may well include further static heat loads not considered here.

In Fig. 8(a) we show the total heat loads as a fraction of the available cooling power at each stage as a function of processor size, using the estimated cooling powers at each stage of a Bluefors XLD1000-SL dilution refrigerator shown in Table I. Fig. 8(b) shows a typical simulation result for 144 qubits, where the origin of the heat loads at each stage is shown in a stacked bar graph. In principle, the system will be able to cool to base temperature provided all stages have less heat load than their nominal

cooling power.

We caution readers that the model does not capture some additional heat loads that will change the results. In particular, the active heat load due to the resistance of the package that holds the processor is not considered here. Other heat loads, such as the presence of a long-life cold trap, can add further static loads to the 50K and 4K stages. As such, this model only captures a general overview, and we use it to demonstrate a system with sufficient engineering margin that could be used as a starting point for a real design. The full configuration and sources of heat would need to be modeled before the authors would have sufficient confidence to recommend any particular design. In addition, the time taken to cool to base temperature may be an important system parameter. This thermal model only considers the steady state case and a more complete model would be needed to determine the cooldown time, which will depend on the mass, heat capacity, and thermal conductances of each item attached to a stage.

Options to improve the thermal performance include replacing the SC-086/50-SCN-CN cable with microwave flex cable that reduces the static load by scaling the cross-sectional area and combining several signals into one assembly or with cables made from other low thermal conductivity metals such as brass or stainless steel. In this case, there is a trade-off between reducing the static load due to lower thermal conductivity and increasing the active load due to higher electrical resistivity. Using a superconducting cable would dramatically reduce the static and active heat loads, particularly between the 4K and the MXC stages. This option is possible at the lower fridge stages below the 4K stage, where the temperatures are below the superconducting transition temperatures of commercially available superconducting cables [28]. The TWPA pump termination resistor could also

be relocated to the cold plate, which has a lower heat load. New designs of kinetic inductance parametric amplifiers operate at 4 K and may be able to replace the current LNA and the TWPA [29]. Optical transduction of the microwave output signal at the mixing chamber [30] is another method that would allow the LNA amplifiers to be removed and replace the microwave readout chain with an optical one. Finally, control lines using optical fibers and transducers to create RF signals at the base of the fridge have also been demonstrated and could potentially replace the coax cables [6].

In addition, the required volume, mass, and mounting infrastructure for typical off-the-shelf readout components such as circulators and TWPA amplifiers could potentially put an upper bound on the number of readout chains that could fit in the MXC, which in turn will put an upper bound on the number of qubits possible for such system. Based on experience with the current hardware size, it would be challenging to accommodate more than the 24 readout lines required for the 144-qubit processor on the mixing chamber of a Bluefors XLD1000-SL system.

## VI. CONCLUSION

We measured the thermal conductivity and electrical resistivity of SC-086/50-SCN-CN coaxial cables from room temperature to approximately 4 K. This data was then used to create smooth functions of each respective property with temperature, using simple approximations to extend the fits beyond the experimental data down to the millikelvin regime. We then used these functions to calculate static and active heat loads for a superconducting quantum processor in a dilution fridge in realistic configurations. Finally, we applied these thermal models to a set of hypothetical model flux tunable superconducting transmon processors of increasing size. The model processors use the tunable coupler architecture, and so each transmon requires two signal lines (an XY control and a flux bias line), while the tunable couplers require a flux bias line. The readout system is also modeled, including TWPA amplifiers at the mixing chamber and semiconductor LNA amplifiers at the 4K stage. For a Bluefors XLD1000-SL dilution refrigerator using HDW wiring, the theoretical limit of the system using all the available cooling power is approximately 200 qubits. However, with engineering margin in the cooling power and the available space for microwave readout circuitry at the mixing chamber, the practical limit is approximately 140 qubits.

## VII. ACKNOWLEDGEMENTS

We would like to thank Jen-Hao Yeh, Sanya Deshpande, and Michael Selvanayagam for their guidance in the early stages of this project.

This work was produced by Fermi Research Alliance, LLC under Contract No. DE-AC02-07CH11359 with the U.S. Department of Energy. Publisher acknowledges the U.S. Government license to provide I-238 public access under the DOE Public Access Plan (<https://www.energy.gov/doe-public-access-plan>).

- 
- [1] J. Clarke and F. K. Wilhelm, *Nature* **453**, 1031 (2008).
- [2] S. Krinner, S. Storz, P. Kurpiers, P. Magnard, J. Heinsoo, R. Keller, J. Lütolf, C. Eichler, and A. Wallraff, *EPJ Quantum Technology* **6**, 1 (2019).
- [3] S. Deshpande, J.-P. Paquette, M. Vahidpour, M. Selvanayagam, R. Lion, M. Pelstring, S. Caldwell, M. Reagor, and D. Russell, in *2019 IEEE MTT-S International Microwave Symposium (IMS)* (2019) pp. 271–274.
- [4] A. Potočnik, S. Brebels, J. Verjauw, R. Acharya, A. Grill, D. Wan, M. Mongillo, R. Li, T. Ivanov, S. V. Winckel, F. A. Mohiyaddin, B. Govoreanu, J. Craninckx, and I. P. Radu, *Quantum Science and Technology* **7**, 015004 (2021).
- [5] S. Pellerano, S. Subramanian, J.-S. Park, B. Patra, T. Mladenov, X. Xue, L. M. K. Vandersypen, M. Babaie, E. Charbon, and F. Sebastiano, in *2022 IEEE Custom Integrated Circuits Conference (CICC)* (2022) pp. 01–08.
- [6] F. Lecocq, F. Quinlan, K. Cicak, J. Aumentado, S. A. Diddams, and J. D. Teufel, *Nature* **591**, 575 (2021).
- [7] K. Uhlig, *Cryogenics* **42**, 73 (2002).
- [8] K. Uhlig, *AIP Conference Proceedings* **985**, 1287 (2008).
- [9] Bluefors, “XLD-SL dilution refrigerator measurement system,” <https://bluefors.com/products/dilution-refrigerator-measurement-systems/xldsl-dilution-refrigerator-measurement-system/> (2025), retrieved on 2025-01-16.
- [10] F. Yan, P. Krantz, Y. Sung, M. Kjaergaard, D. L. Campbell, T. P. Orlando, S. Gustavsson, and W. D. Oliver, *Phys. Rev. Applied* **10**, 054062 (2018).
- [11] E. D. Marquardt, J. P. Le, and R. Radebaugh, in *Cryocoolers 11*, edited by R. G. Ross (Springer US, Boston, MA, 2002) pp. 681–687.
- [12] Bradley, P.E., Radebaugh, R., and Lewis, M.A., in *Proceedings of ICMC '06 Twenty First International Cryogenic Engineering Conference and 9th Cryogenics* (Icaris, Prague, CZ, 2006) pp. 13–21.
- [13] CoaxCo, “SC-086/50-SCN-CN,” <http://www.coax.co.jp/en/product/sc/086-50-scn-cn.html>, retrieved on 2024-03-01.
- [14] O. Maldonado, *Cryogenics* **32**, 908 (1992).
- [15] “Quantum Design North America - PPMS TTO Manual B0,” <https://qdusa.com/pharosindex/> ().
- [16] S. I. Woods, T. M. Jung, D. R. Sears, and J. Yu, *Cryogenics* **60**, 44 (2014).
- [17] K. Gelin and E. Wäckelgård, *Journal of Physics: Condensed Matter* **16**, 833 (2004).
- [18] Bluefors, “High-density wiring,” <https://bluefors.com/products/measurement-infrastructure/high-density-wiring/> (2021), retrieved on 2024-03-01.
- [19] A. Vaaranta, M. Cattaneo, and R. E. Lake, *Physical Review A* **106**, 042605 (2022).
- [20] S. Simbierowicz, M. Borrelli, V. Monarkha, V. Nuutinen, and R. E. Lake, *PRX Quantum* **5**, 030302 (2024).
- [21] J.-H. Yeh, J. LeFebvre, S. Premaratne, F. C. Wellstood, and B. S. Palmer, *Journal of Applied Physics* **121**, 224501 (2017).
- [22] S. Simbierowicz, V. Y. Monarkha, S. Singh, N. Messaoudi, P. Krantz, and R. E. Lake, *Applied Physics Letters* **120**, 054004 (2022).
- [23] C. Macklin, K. O’Brien, D. Hover, M. E. Schwartz, V. Bolkhovskiy, X. Zhang, W. D. Oliver, and I. Siddiqi, *Science* **350**, 307 (2015).
- [24] Bluefors, “Microwave readout module,” <https://bluefors.com/products/measurement-infrastructure/microwave-readout-module/> (2024), retrieved on 2024-11-15.
- [25] LowNoiseFactory, “LNF-LNC4.8G amplifier,” <https://lownoisefactory.com/product/lnf-lnc4.8g/> (2024), retrieved on 2024-11-15.
- [26] K. O’Brien, C. Macklin, I. Siddiqi, and X. Zhang, *Physical Review Letters* **113**, 157001 (2014).
- [27] D. C. Feng, M. Vahidpour, Y. Mohan, N. Sharac, T. Whyland, S. Stanwyck, G. Ramachandran, and M. Selvanayagam, in *2020 IEEE/MTT-S International Microwave Symposium (IMS)* (2020) pp. 940–943.
- [28] “Cri/oFlex® 3 | Flexible RF Multi Channel | Cryo Multi RF,” <https://delft-circuits.com/product-overview/cf3/> ().
- [29] M. Malnou, M. Vissers, J. Wheeler, J. Aumentado, J. Hubmayr, J. Ullom, and J. Gao, *PRX Quantum* **2**, 010302 (2021).
- [30] T. C. van Thiel, M. J. Weaver, F. Berto, P. Duivestijn, M. Lemang, K. L. Schuurman, M. Žemlička, F. Hijazi, A. C. Bernasconi, E. Lachman, M. Field, Y. Mohan, F. K. de Vries, C. C. Bultink, J. van Oven, J. Y. Mutus, R. Stockill, and S. Gröblacher, “Optical readout of a superconducting qubit using a scalable piezo-optomechanical transducer,” (2023), arXiv:2310.06026 [quant-ph].